Three-dimensional optical forces and transfer of orbital angular momentum from multiringed light beams to spherical microparticles

Karen Volke-Sepúlveda

Instituto de Física, Universidad Nacional Autónoma de México, Apartado Postal 20-364, 01000 México Distrito Federal, México

Sabino Chávez-Cerda

Instituto Nacional de Astrofísica, Optica y Electrónica, Apartado Postal 51/216, Puebla, Puebla 72000, México

Veneranda Garcés-Chávez and Kishan Dholakia

School of Physics and Astronomy, University of St. Andrews, North Haugh, St. Andrews, Fife KY16 9SS, Scotland

Received September 8, 2003; revised manuscript received April 27, 2004; accepted May 6, 2004

Experimental evidence of transfer of orbital angular momentum of multiringed beams to dielectric particles has been reported recently [e.g., J. Opt. B **4**, S82 (2002); Phys. Rev. Lett. **91**, 093602 (2003)]. Here we present a detailed theoretical examination of the forces involved in trapping and transferring orbital angular momentum to microparticles due to a multiringed light beam, particularly a Bessel beam. Our investigation gathers, in a more general way, the trapping forces for high-index and low-index dielectric transparent particles, as well as for reflective metallic particles, as a function of particle size and position relative to the dimensions of the rings of the beam. We find that particles can be trapped in different regions of the beam intensity profile according to their size and that an azimuthal force component opposite to the beam helicity may appear under certain circumstances, depending on the relative size and radial equilibrium position with respect to the beam for high-index spheres. © 2004 Optical Society of America

OCIS codes: 140.7010, 290.5850, 080.2720, 140.3300.

1. INTRODUCTION

It was demonstrated in 1992 that Laguerre–Gaussian (LG) laser modes carry orbital angular momentum (OAM). This arises because the Poynting vector and the linear momentum density of these beams have an azimuthal component.[1] More recently, the Poynting vector and the orbital angular momentum of high-order Bessel beams (BBs) have been analyzed.[2,3] Bessel beams are propagation-invariant optical fields and may retain this property for very long distances in contrast to focused LG beams that spread rapidly owing to diffraction.[4,5] The transverse intensity profile of the former beams consists of a large number of concentric bright rings limited only by the optics of the experimental setup, while the profile of LG beams has a finite number of rings that is determined by a radial index.

Optical tweezers allow the confinement of dielectric and metallic particles in three dimensions and analysis of their subsequent motion by use of the gradient force.[6] As such, they offer an excellent mechanism to probe the spin and orbital angular momentum of multiringed LG and Bessel light beams. As proof of this, in 1995, transfer of OAM from a LG beam to absorbing particles was experimentally demonstrated for the first time,[7] and, subsequently, studies relating both spin and OAM with such systems followed.[8,9] Later, in 2002, the first experiments verifying OAM transfer from Bessel light beams were reported.[3,10] By the mechanism of scattering, both kinds of dielectric particles, high and low index, were trapped and rotated.

Depending upon where a particle is placed within a beam possessing OAM, the particle can rotate around its own axis or around the axis of the light beam; this has been used to define the intrinsic and extrinsic nature of the light.[11,12] These different manifestations of the OAM of a light beam can only be observed separately. However, if the intrinsic spin angular momentum is also involved, it is possible to observe both of them simultaneously in a multiringed beam.[13]

While these experiments have given significant insights into OAM of light, theoretical studies have been relatively limited. Although several numerical models can be found in the literature to describe the magnitude and direction of the optical forces,[14–19] it was only recently that multiringed light beams and the OAM transfer process started to be investigated.[10] An advantage of multiringed beams is that they offer more flexibility than single-ringed beams for studies of angular momentum of light, and the use of Bessel beams allows the potential of investigating even in the nonparaxial regime.[3]

The models based on geometrical optics provide highly reliable results within the limits of validity of this theory. In a geometrical-optics picture, light rays have the form of straight lines in propagation through a homogeneous and

0740-3224/2004/101749-09$15.00

linear medium. However, the light rays can be defined in a broader and rigorous way as oriented curves whose direction coincides everywhere with the direction of the Poynting vector, providing information about the magnitude and direction of the energy flow and the linear and angular momenta of the field.[20] This approach has been suggested as an adequate alternative to analyze the case of beams carrying OAM.[12,20,21] This fact has been used in a previous work where a model using skewed rays to make a quantitative analysis of the OAM transfer process was developed, but it was restricted to analyze low-index dielectric particles only,[10] and several aspects remained unexplored.

In this paper, we perform a detailed study of the three-dimensional optical forces due to multiringed beams acting on the process of trapping and transfer of OAM to dielectric transparent spheres of high and low relative refractive index, and also to highly reflective metallic particles. We particularly look at Bessel light beams but stress that the results can also be applied to other multiringed beams such as high radial order LG beams and elliptical Mathieu beams.[22]

The structure of the paper is as follows: First, we analyze the axial optical force exerted by a lowest-order Bessel beam on a high-index dielectric sphere, and we compare it with the corresponding force exerted by a Gaussian beam to analyze the phenomenon of optical guiding. Second, for the three kinds of particles mentioned above, we study the radial force exerted by high-order BBs, which defines the equilibrium positions in different regions in the radial direction of the multiringed transverse intensity pattern. Finally, we look at the tangential force generated by the scattering of the azimuthal component of the Poynting vector, which gives rise to the rotation of the particles around the beam axis. Our findings allow us to make new predictions concerning the radial equilibrium positions of the particles as a function of their relative size with respect to the beam dimensions and the corresponding azimuthal forces.

2. THEORETICAL MODEL FOR ANGULAR-MOMENTUM TRANSFER

The model used in the present work to compute the optical forces has been developed in detail elsewhere.[23] We will present here only its most relevant features necessary to introduce the main parameters and include some additional details in the appendix.

The total optical force $\mathbf{F}$ acting on a transparent sphere can be expressed as[17,23]

$$\mathbf{F} = \frac{1}{v_m}\int_S I(\mathbf{r})\cos\alpha_i(\mathbf{r})\Bigg[\hat{\mathbf{u}}_i(\mathbf{r}) - R(\mathbf{r})\widehat{\mathbf{u}_r}(\mathbf{r}) - T(\mathbf{r})^2\sum_{k=1}^{N} R(\mathbf{r})^{k-1}\hat{\mathbf{u}}_{tk}(\mathbf{r})\Bigg]\mathrm{d}A. \qquad (1)$$

Here v_m is the light velocity in the medium surrounding the particle, $I(\mathbf{r})$ is the intensity distribution of the incident field, α_i is the incidence angle with the normal at the incidence point, $\mathrm{d}A$ is the surface element of the sphere, and S is the part of the sphere's surface that is illuminated by the incident field. $\hat{\mathbf{u}}_i$ is a unit vector in the direction of the incident ray, whereas $\widehat{\mathbf{u}_r}$ is a vector in the direction of the reflected ray at the incidence point $\mathbf{r}$. The vector $\hat{\mathbf{u}}_{tk}$ corresponds to the ray transmitted out of the sphere after k internal reflections, and N is the maximum number of internal reflections that a light ray suffers before leaving the sphere; we have set $N = 20$, which guarantees convergence to the case $N \to \infty$.[10] Finally, the proportion of the reflected and transmitted light each time is calculated with the reflection and transmission Fresnel coefficients R and T, respectively.

For the intensity distribution of the incident light beam $I(\mathbf{r})$, we will consider a Bessel beam of arbitrary order. When an axicon is illuminated with a vortex field, a high-order BB is generated with the same topological charge. The three-dimensional intensity distribution of an lth-order Bessel beam generated in this way can be approximated by using the method of stationary phase applied to the corresponding Fresnel diffraction integral, which yields[24]

$$I_l(\rho,\ \varphi,\ z) = \frac{2^{l+2}}{l!}\left(\frac{k_t P}{w_c}\right) \times\left(\frac{z}{z_{\max}}\right)^{2l+1} J_l^2(k_t\rho)\exp(-2z^2/z_{\max}^2), \qquad (2)$$

where P is the total power of the beam, k_t is the transverse component of the wave vector, w_c is the beam waist associated with a well collimated single-ringed LG beam incident upon the axicon, and $z_{\max} = kw_c/k_t$ is the maximum propagation distance of the beam, with k being the wave number. It is seen from Eq. (2) that, although the transverse beam profile remains unchanged, its intensity varies along the propagation axis, having a maximum at some point. The peak of the intensity of the propagating high-order BB is at $z_{\text{peak}} = (\sqrt{2|l| + 1}/2)z_{\max}$, and this is the plane where the transverse optical forces will be evaluated.

On the other hand, the vector associated with the incident light ray is proportional to the linear-momentum density of the illuminating beam. In general, the ratio of the linear momentum density to the intensity, or the momentum contribution per photon for beams that possess OAM, can be expressed as

$$\frac{\langle\mathbf{g}(\mathbf{r})\rangle}{I_l(\mathbf{r})} = f_\rho(\mathbf{r})\hat{\boldsymbol{\rho}} + f_\varphi(\mathbf{r})\hat{\boldsymbol{\varphi}} + f_z(\mathbf{r})\hat{\mathbf{z}}, \qquad (3)$$

$\hat{\boldsymbol{\rho}}$, $\hat{\boldsymbol{\varphi}}$, and $\hat{\mathbf{z}}$ being the unit vectors in the radial, azimuthal, and axial directions, respectively, in the reference frame of the beam. The functions f_ρ, f_φ, and f_z are well determined for BBs[3]; in particular, for a linearly polarized BB in the paraxial regime, we have

$$f_\rho(\mathbf{r}) = 0, \quad f_\varphi(\mathbf{r}) = \frac{l}{k\rho}, \quad f_z(\mathbf{r}) = \cos\gamma, \qquad (4)$$

where γ is the cone angle of the Bessel beam, defined by $\tan\gamma = (k_t/k_z)$, with k_z being the axial component of the wave vector. The azimuthal component of the linear momentum density is what gives rise to contributions of the net optical force in the azimuthal direction, and that is the basis of the OAM transfer by scattering.

Then the total three-dimensional optical force can be written in terms of $\mathbf{F}^{(\rho)}$, $\mathbf{F}^{(\varphi)}$, and $\mathbf{F}^{(z)}$, which denote the respective contributions due to the radial, azimuthal, and axial components of the incident light rays. It is necessary to treat all these contributions separately, since the integration limits are different in each case. For Bessel beams, $\mathbf{F}^{(\rho)} = 0$, and the explicit expressions used to calculate the components of the forces $\mathbf{F}^{(\varphi)}$ and $\mathbf{F}^{(z)}$ along the x', y', and z' axes associated with the reference frame of the sphere are given in the appendix. Finally, in order to identify the components of the net optical force in respect to the reference frame of the beam, we can write $\mathbf{F} = F_\rho \hat{\boldsymbol{\rho}} + F_\varphi \hat{\boldsymbol{\varphi}} + F_z \hat{\mathbf{z}}$, where $F_\rho \equiv F_{x'}^{(\varphi)} + F_{x'}^{(z)}$, $F_\varphi \equiv F_{y'}^{(\varphi)}$, and $F_z \equiv F_{z'}^{(z)}$, since the x' and y' axes coincide with the radial and azimuthal directions of the frame *xyz*, respectively. In addition, the corresponding optical torques can be calculated from the expressions for the optical forces acting on the sphere.

This model is also suitable to analyze the case of highly reflective metallic particles with negligible absorption, for which the reflection and transmission Fresnel coefficients are taken simply as $R = 1$ and $T = 0$ for any value of the incidence angle.

3. NUMERICAL RESULTS

In this section, we present and discuss some numerical results for the trapping forces and angular-momentum transfer for three different kinds of particles: high-index dielectric spheres ($n > 1$, where n is the relative refractive index of the particle with respect to the surrounding medium), low-index dielectric spheres ($n < 1$), and highly reflective metallic particles. The three-dimensional forces in a cylindrical reference frame will be analyzed. We start with a brief analysis of the axial optical force in which we compare a BB with a Gaussian beam, and then we analyze the transverse forces. The radial forces define the equilibrium regions where the particles can be trapped radially within the beam intensity profile. We end our analysis by looking at the azimuthal forces. We have paid attention in using numerical values corresponding to typical experimental ones; nevertheless, we will present our results in terms of dimensionless parameters.

A. Axial Optical Force: Optical Guiding

Owing to the lack of a strong intensity gradient in the axial direction, it is not possible to trap particles in three dimensions with an unfocused BB. However, BBs have been used efficiently to transport particles along extended distances,[25] which is also known as optical guiding. In order to appreciate this fact more clearly, we will establish a comparison between the axial optical forces exerted by a zero-order Bessel beam and a Gaussian beam.

The radius of the central bright spot of the BB is chosen to be the same as the waist spot size of the Gaussian beam, w_0. In terms of the Bessel-beam parameters, this simply corresponds to $\sin \gamma = x_0/kw_0$, where $x_0 = 2.4048$ is the first zero of the Bessel function $J_0(x)$. The direction of the incident light rays is taken to be parallel to the propagation axis for both beams, which is a reasonable assumption for optical guiding. The axial optical force for the Gaussian beam is calculated by means of expression (10) of the appendix by setting $f_z(\mathbf{r}) = 1$, and in this case the corresponding intensity distribution is $I(\mathbf{r}) = [2P_0/\pi w^2(z)]\exp[-2\rho^2/w^2(z)]$, where $w^2(z) = w_0^2[1 + (z/z_R)^2]$ and $z_R = kw_0^2/2$ represents the Rayleigh range of the Gaussian beam. The beam-waist plane is set to the position $z_{\text{peak}} = z_{\max}/2$, which corresponds to the peak on-axis intensity of the BB along its maximum propagation distance.

Typically, low-index particles and metallic spheres may not be confined in a Gaussian beam[26] (this point will become clearer when we study the transverse optical forces), so we analyze a silica sphere immersed in water ($n = 1.087$ at $\lambda_0 = 518$ nm) whose radius is given by $R_0 = 1.5\,w_0$.

The axial forces for both beams are plotted against the parameter z_0/z_R in Fig. 1, where z_0 is the distance from the axicon vertex to the sphere. The Bessel-beam parameters are set such that its maximum propagation is $z_{\max} = 40\,z_R$, and its total power is $P = 4\,P_0$, where $P_0 = 1$ mW is the unit power for the Gaussian beam (for higher power, the plots just scale). The total power of the BB needs to be higher than the Gaussian beam because it is uniformly distributed among all the rings in the transverse intensity distribution. In general, the larger the maximum propagating distance of the Bessel beam, the more power required for optical guiding, but a larger guiding distance is created.

We can see from Fig. 1 that, although the peak force is larger for the Gaussian beam (for comparison, the particle's weight is ~0.27 pN), the BB maintains the force over a longer distance. The shape of the curve for the Gaussian beam means the particle may have a wide variation in its velocity along the guiding range, and even when it

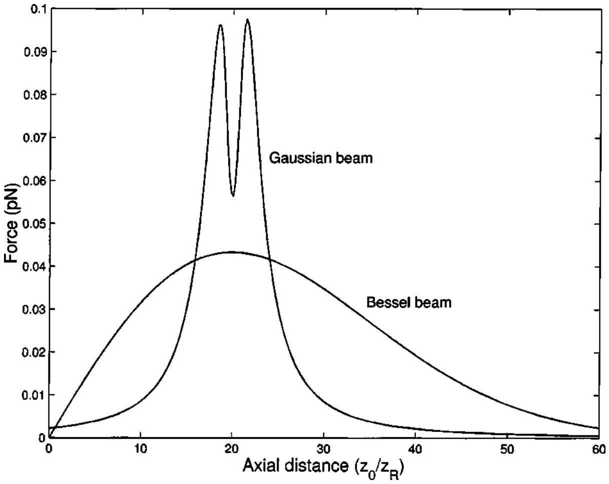

Fig. 1. Comparison of the axial optical forces exerted on a silica sphere immersed in water ($n = 1.087$) by a Bessel beam and by a Gaussian beam. The parameters for the beams are the following: the radius of the central bright spot of the Bessel beam is $\rho_B = 0.9\,w_0$, its maximum propagation distance $z_{\max} = 40\,z_R$, and its total power $P = 4\,P_0$, where w_0 is the waist spot size of the Gaussian beam, z_R is its Rayleigh range in the medium, and $P_0 = 1$ mW is its total power. The radius of the sphere is $R = 1.5w_0$. These curves are exactly the same regardless of the specific value of w_0 and the wavelength of the laser light, provided the ratios between the parameters of both beams and with the size of the particle are preserved.

reaches a terminal velocity at some point, this will fall off rapidly owing to the beam spreading. The two maxima are associated with the positions where the beam spot size approximates the sphere's size, $w(z_0)/R_0 \approx 1$; thus their locations in respect to the beam waist shift outward for larger particles, but their magnitudes remain approximately the same. If the particle is smaller than the beam-waist spot ($R_0 < w_0$), its lower hemisphere is always completely illuminated by the beam, and there is only one maximum of the force located at the beam-waist plane.

On the other hand, in the case of the BB, the particle is expected to reach a terminal velocity and maintain it within a longer distance, since the force variations are much smoother. The general behavior of the curve is the same regardless of the size of the particle, but the magnitude of the force increases for larger spheres owing to the higher amount of light reaching the particle.

This example illustrates the advantages of Bessel beams for optical guiding, which is in contrast to the suitability of strongly focused Gaussian beams to achieve three-dimensional optical confinement.[6] In fact, in the angular-momentum transfer experiments with BBs, the particles are trapped in the vertical direction by pushing them against a surface by the axial optical force,[3] but in that case, the fundamental role is played by the transverse optical force, constituted by its radial and azimuthal components.

B. Radial Optical Force: Transverse Trapping

An interesting feature of multiringed light beams is that their alternate bright and dark regions allow the confinement of different types of particles (the details of forces for each of these are given in the appendix). This is shown in Fig. 2, where we have plotted the radial forces F_ρ for a Bessel beam for three kinds of spheres as a function of the parameter $r = \rho_0/\rho_1$, where ρ_1 is the radius of the first intensity maximum of the beam. The black solid curve corresponds to a high-index dielectric sphere; the dashed curve is for a low-index particle, and the dash-dotted curve describes the case of a metallic particle. The corresponding intensity profile is also included in the figure as a reference (gray solid curve).

The equilibrium positions in the radial direction are defined by the condition $F_\rho(r) = 0$, and they are stable when the slope of the curve is negative, since for any displacement in a determined direction, there is a restoring force in the opposite direction that confines the particle in those points. It is seen from the figure that the stable equilibrium positions are located at the intensity maxima of the beam for the silica sphere, while these are located in the dark regions for low-index and metallic particles. This is in agreement with experimental observations.[3,10]

It is clear from Fig. 2 that the magnitude of the optical forces is larger for the low-index than for the high-index sphere. This is because the deflection of the light, which is connected with the change in the linear momentum, is higher for reflected than for refracted light rays, and in the case of low-index spheres, the reflection coefficients are larger than the transmission coefficients for a wide range of values of the incidence angle, reaching the value of $R = 1$ when the total internal reflection occurs. This fact is even more evident for the case of metallic spheres, which reflects all the incident light, giving rise to the largest optical forces.

By analyzing the variation of the radial forces as the diameter of the particles increases, we found that the equilibrium positions shift toward the beam center for high-index particles and outward from the beam axis in the other two cases (except the equilibrium position at the dark center of the beam). In fact, this behavior depends on the relative size of the particle with respect to the beam dimensions, which we characterize in terms of a size parameter $\alpha = R_0/\rho_1$. We observed then that, the larger the value of α is, the more the equilibrium positions shift. In the three cases, there exist critical values of the size parameter for which the spheres can be held at the beam center, whereas the outer equilibrium positions either become very weak or even disappear. In the case of the high-index sphere, that situation corresponds to a displacement of 100% of the first equilibrium position in respect to its original location at the first intensity maximum. For example, for a Bessel beam of order $l = 2$, this occurs for $\alpha > 1.21$.

The shift percentage for the stable equilibrium position associated with the first bright ring in the case of high-index particles (solid curve), and with the first dark ring in the cases of low-index (dashed curve) and metallic (dash-dotted) particles, is plotted in Fig. 3 against the size parameter of the sphere α, for a BB of helicity $l = 2$. The curves for the low-index and metallic spheres are cut off when $\alpha = 0.78$ and $\alpha = 0.84$, respectively, because for larger values of α, the corresponding equilibrium positions disappear.

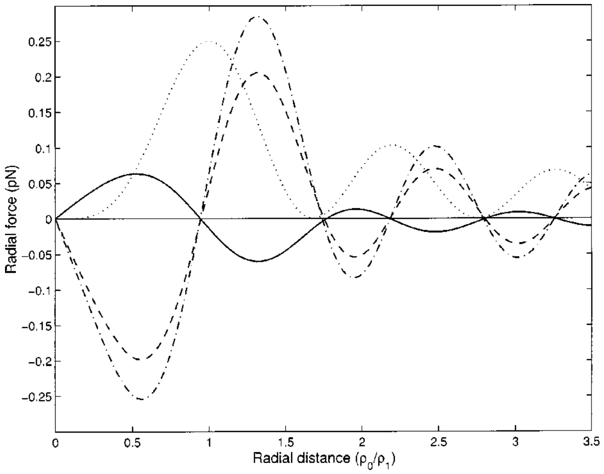

Fig. 2. Radial optical force per unit power exerted by a Bessel beam with helicity $l = 2$ and $z_{\max} = 100\ \mu$m on three different kinds of spheres as function of the dimensionless parameter $r = \rho_0/\rho_1$, where ρ_0 is the distance from the beam center and ρ_1 is the radius of the first intensity maximum of the beam. The solid black curve corresponds to a high index dielectric sphere (a silica particle in water, $n = 1.087$), the dashed curve is for a low-index sphere (a hollow sphere in water $n = 0.7502$), and the dash-dotted curve is for a reflective metallic sphere. All of them have the same radius, $R_0 = 0.6\ \rho_1$. The beam intensity profile is also depicted with a dotted curve as a reference. The parameter $z_{\max}$ determines the magnitude of the forces per unit power, since the larger the value of $z_{\max}$, the lower the magnitude of the forces. However, the shape of the curves is completely independent of the specific value of ρ_1.

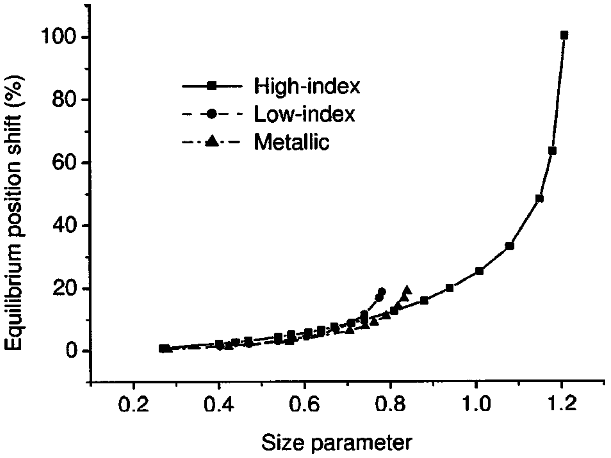

Fig. 3. Percentage of displacement of the radial equilibrium positions with respect to the first intensity maximum in the case of the high-index sphere (solid curve) and with respect to the first dark ring in the cases of low-index (dashed curve) and metallic (dash-dotted curve) spheres, as a function of the size parameter of the particles $\alpha = R_0/\rho_1$.

In order to interpret the shifting in each case, we note that the bright rings of the intensity profile of the BBs are modulated by an envelope curve that behaves as $1/\rho$. When the size of the particles becomes far larger than the average width of the bright rings, the detailed structure of the beam is barely distinguished, and the shape of the envelope starts to dominate the behavior of the particles. Therefore the shifts of the equilibrium positions are the result of the imbalance between the intensity of consecutive bright rings, which pulls the high-index particles toward the regions where the intensity is higher in terms of the envelope (the beam center). The low-index and metallic particles are pushed toward the regions where the envelope of the intensity is lower (outward from the beam center). When a high-index particle is large enough, it rather perceives the beam as a smooth profile with a global maximum at the center. And of course, the same is true for the low-index and metallic spheres, but in these cases, the particles whose size exceed a certain upper limit cannot be trapped by the beam anymore. For a low-index particle interacting with a BB of azimuthal index $l = 2$, the upper size limit is given by $\alpha = 1.28$, whereas in the case of a metallic particle, the limit is $\alpha = 1.37$.

To illustrate how the first equilibrium position moves toward the beam center for high-index particles, we depict in Fig. 4 the radial optical force for silica spheres of radii defined by $\alpha = 1.1$ (solid curve), $\alpha = 1.15$ (dashed curve), and $\alpha = 1.21$ (dash-dotted curve). In the first two cases, the stable equilibrium position is neither at the beam center nor at the first intensity maximum, but at some point between them, whereas in the last case, the only remaining equilibrium position is exactly at the beam center. This result means that particles can actually be trapped not only in the brightest or darkest regions, but in different regions of the intensity profile, depending on their relative size with respect to the beam's transverse dimensions. This is closely related to recent works on sorting particles according to their size in an optical potential.[27,28]

C. Azimuthal Optical Force: Rotation

When $l \neq 0$, the OAM content of a BB may be transferred by means of scattering to particles trapped off-axis. In Fig. 5, we can see the azimuthal optical force F_φ against the radial parameter $r = \rho_0/\rho_1$ for a Bessel beam with the same parameters as in Fig. 2.

A new relevant result for high-index spheres deduced from Fig. 5 is that the azimuthal force is negative at distances close to the beam center. In most cases, the azimuthal force would be positive at the radial position of stable equilibrium of the particles, but, considering the shift of the equilibrium positions toward the beam center for large spheres, according to our model, it is indeed possible to observe a particle rotating in the direction opposite to the beam helicity. For example, for a BB with $l = 2$, whose first intensity maximum is at $\rho_1 = 3.5\ \mu\text{m}$, it should be possible in principle to trap and rotate an 8-μm-diameter silica sphere suspended in water in the direction opposite to the beam helicity. Of course, appropriate sets of experimental parameters can also be found to observe this kind of behavior for other values of the azimuthal index $l \neq 0$.

To understand this fact, we have analyzed the contributions of the reflected and transmitted azimuthal rays separately. We have found that the force on the particle caused by the transmitted rays has a negative azimuthal component when the sphere is close to the center of the beam, but it becomes positive when the sphere gets farther away. In contrast, the contribution of the reflected rays to the azimuthal force is always positive, regardless of where the sphere is located. However, for a value of the relative refractive index close to unity, the transmission coefficients are far larger than the reflection coefficients in a wide range of incidence angles, which means that the transmitted rays have a predominant influence on the total force in that case. As the relative refractive index increases, the transmission coefficients become smaller, and therefore the magnitude of the negative azimuthal force decreases. This can be appreciated from

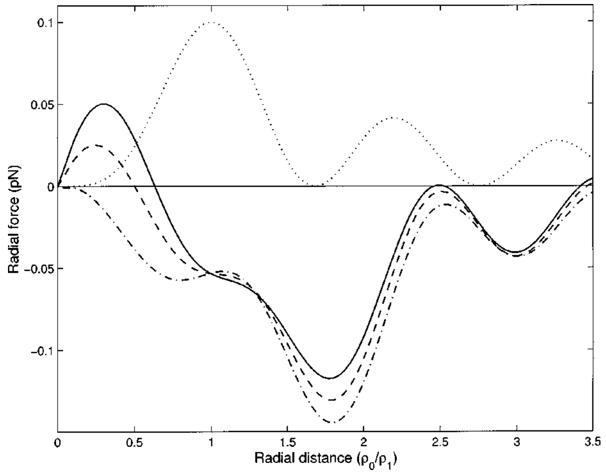

Fig. 4. Radial optical force exerted by a BB with helicity $l = 2$ and $z_{\max} = 100\ \mu\text{m}$ on high-index spheres ($n = 1.087$) whose radii are defined by $R_0 = \alpha\,\rho_1$, with $\alpha = 1.1$ (solid curve), $\alpha = 1.15$ (dashed curve), and $\alpha = 1.21$ (dash-dotted curve). The dotted curve represents the corresponding intensity profile.

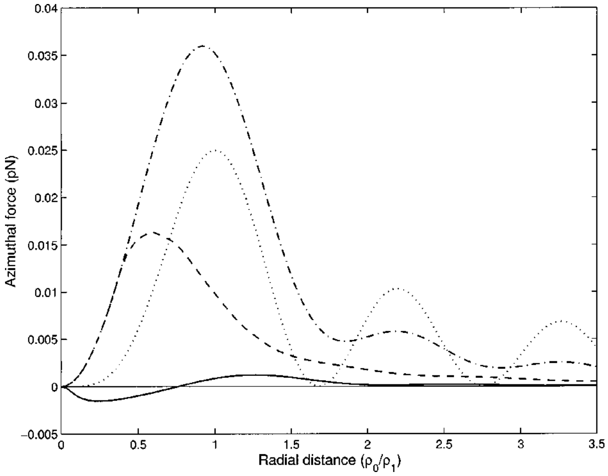

Fig. 5. Azimuthal optical force as a function of $r = \rho_0/\rho_1$ for the three kinds of spheres: high-index (black solid curve), low-index (dashed curve), and metallic particles (dash-dotted curve), for the same parameters as in Fig. 2. The dotted curve represents the corresponding beam profile.

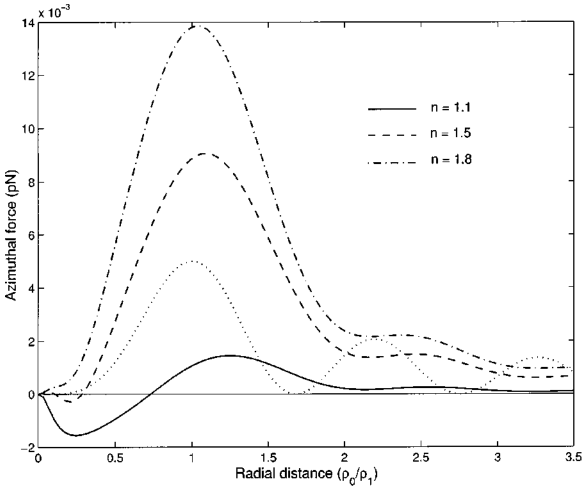

Fig. 6. Intensity profile (dotted curve) and azimuthal optical force per unit power against $r = \rho_0/\rho_1$ for spheres with radius $R_0 = 0.6\,\rho_1$ with relative refractive indices $n = 1.1$ (solid curve), $n = 1.5$ (dashed curve), and $n = 1.8$ (dash-dotted curve), and the same beam parameters as in Fig. 2.

Fig. 6, where the azimuthal optical force acting on a high-index sphere is depicted for different values of the relative refractive index.

In contrast, in the cases of low-index and metallic particles, the azimuthal force is always positive, independently of the sphere's radius and location within the beam profile. This is because for low-index particles, the contributions to the optical force from both the reflected and the transmitted light are always positive.

Vector diagrams showing the vortex distribution of the azimuthal forces within the beam profile for each of the different particles are depicted in Fig. 7. The diagrams of Figs. 7(b), 7(c), and 7(d) correspond to high-index, low-index, and metallic particles, respectively, and the intensity profile of the beam is shown in Fig. 7(a) for comparison.

Having determined the radial equilibrium positions and the azimuthal force acting on a spherical particle, we can calculate its rotation rate from Eq. (11) as a function of the total power of the beam. According to Eqs. (7)–(9) of the appendix, a change in the value of the total power of the beam just scales the plots $F_\rho(r)$ versus r without affecting the equilibrium positions.

Figure 8 shows the theoretical results for the rotation rates of the three kinds of particles against the total beam power. Notice that, even when the magnitude of the azimuthal force is considerably larger for hollow spheres than for solid spheres, the resulting rotation rates do not differ very much. This is because the rotation rates depend on the ratio of the azimuthal force to the radial position of the particle $[F_\varphi(\rho_0)/\rho_0]$, and the hollow spheres are trapped farther away from the beam center (see the appendix). In the case of the metallic sphere, the slope is much larger, which is evident from the fact that the optical forces are stronger for reflective spheres, while the equilibrium positions are similar to those of the hollow particles.

4. CONCLUSIONS

The three-dimensional forces involved in the optical trapping and manipulation of microscopic particles with multiringed light beams have been thoroughly investigated. Specifically, we analyzed the case of Bessel light beams. The model used is based on the principles of geometrical optics and also incorporates wave theory, such as skew light rays following the trajectory of the Poynting vector for the case of beams possessing orbital angular momentum. This allowed us to model the transfer of OAM through the scattering of the azimuthal component of the linear momentum density for three different kinds of particles: high- and low-index dielectric particles and highly reflective metallic particles.

Axial optical forces exerted by Bessel and Gaussian beams were compared, and it was found that Bessel beams are more appropriate for optical guiding, but this implies that they are not suitable for three-dimensional optical confinement.

Transverse optical forces were analyzed for high-order Bessel beams obtaining formal results that explain experimental observations. For the radial forces, it was found that the high-index particles are attracted to the peak intensity regions, while the low-index and the reflective particles are repelled from them. For this reason, low-index and reflective particles can be manipulated with beam profiles having alternate bright and dark regions, as is the case of multiringed light beams. However, we observed that the radial equilibrium positions of high-index spheres, which are located at the intensity maxima for small particles, start to shift toward the center of the Bessel beam when the diameter of the particles increases with respect to the rings width. In contrast, the radial equilibrium positions associated with the first dark ring and in general with all the outer dark rings, for the case of low-index and metallic spheres, are displaced outward from the beam center as the size of the particles increases. These behaviors were attributed to the fact-that large particles compared with the characteristic dimensions of the beam do not distinguish the ringed structure of the beam profile, and thus they act as if the beam

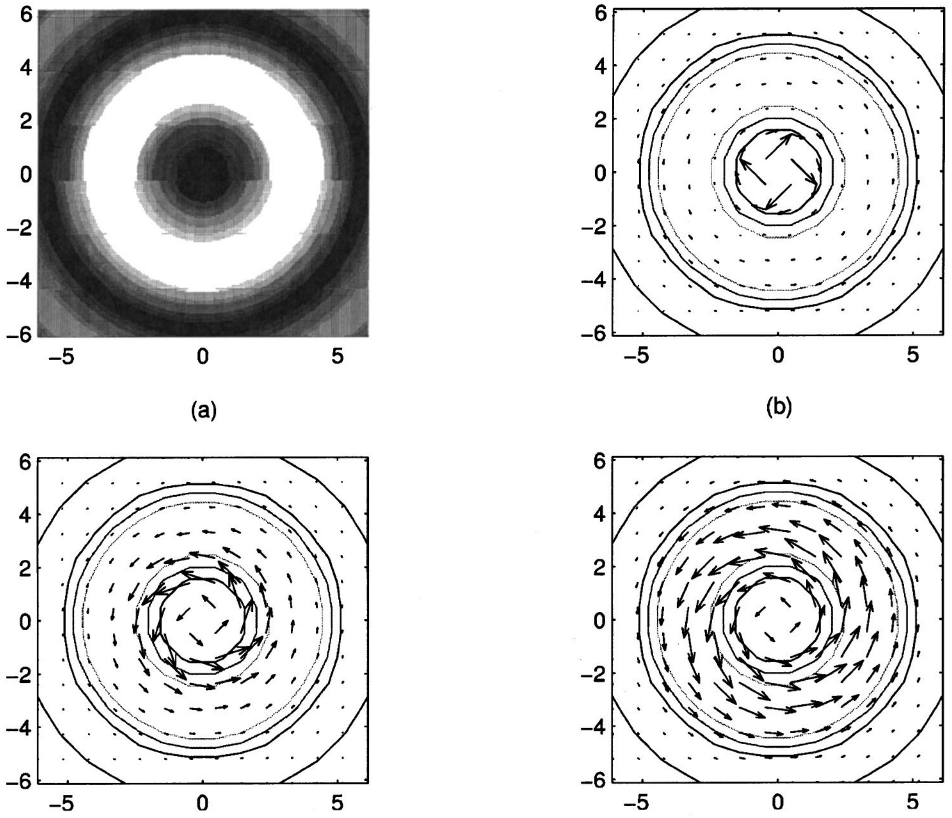

(a) (b) (c) (d)

Fig. 7. Vector diagrams of the azimuthal optical force for the same parameters as in Fig. 2: (a) Intensity profile of the BB. Cases of (b) high-index dielectric sphere, (c) low-index dielectric sphere, and (d) metallic sphere.

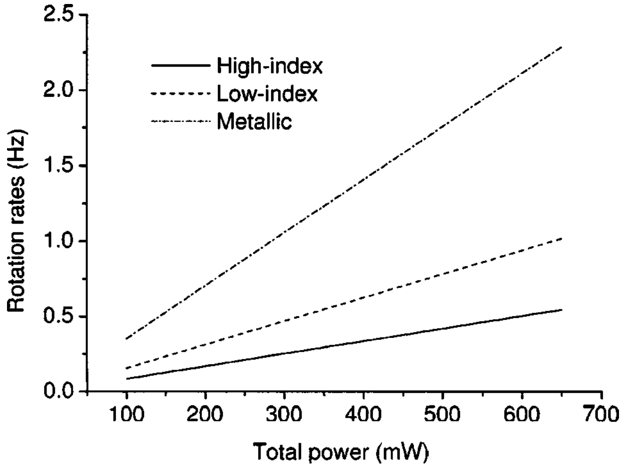

Fig. 8. Rotation rates against the total incident power for the silica (solid curve), hollow (dashed curve), and silver (dash-dotted curve) spheres immersed in water. We consider silica, hollow, and silver spheres immersed in water with radii $R_0 = 0.6\,\rho_1$, and for the Bessel beam we have $l = 2$ and $z_{\max} = 100\ \mu\text{m}$. We assume a viscosity coefficient for water of $\eta = 1.0 \times 10^{-3}\ \text{N s m}^{-2}$, which corresponds to a temperature of 20 °C.

had a smooth profile with a maximum in the center. In that sense, we conclude that the radial trapping positions of the different particles are not restricted to the highest or lowest intensity regions, but they may be in different regions, depending on the relative size of the particles with respect to the beam transverse dimensions. This result is related to recent research on microfluidic sorting of particles according to their size in an optical potential.[27,28]

Regarding the azimuthal optical force, it was found that, with appropriate conditions, high-index spheres trapped at a near distance from the beam center could rotate in the opposite direction to the beam helicity. This is because the azimuthal force can be negative for relatively large particles, since the refracted light has a negative contribution that may exceed the positive contribution of the reflected rays.

We also found that the magnitude of the optical forces is the largest for the case of highly reflective metallic particles, and hence the angular-momentum transfer by scattering is expected to be more efficient for this kind of particle than for the other two cases. Furthermore, we made a quantitative comparison for the rotation rates of the three different kinds of particles finding that, while the rotation rates for the transparent dielectric particles are similar to each other, they are the highest for metallic particles.

We notice that the behavior of other multiringed beams, like LG beams with radial index $p \gg 1$, will be very similar to that of BBs investigated here, regardless of the azimuthal order.

APPENDIX A. EXPRESSIONS FOR THE OPTICAL FORCES AND TORQUES EXERTED BY A BESSEL BEAM

The starting point is to consider two reference frames,[10,23] one associated with the incident light beam (x, y, z) and the other one with the particle (x', y', z'). The equations that relate both reference frames are

$$\rho = (\rho_0^2 + R_0^2\sin^2\theta + 2\rho_0 R_0\sin\theta\cos\phi)^{1/2}, \tag{5}$$

$$z = z_0 + R_0\cos\theta, \tag{6}$$

where R_0 is the radius of the sphere, ρ_0 is the distance between the parallel z and z' axes, ρ denotes the radial distance between the z axis and the incidence point P, z_0 represents the distance between a reference plane $z = 0$ and the center of the sphere at the origin of the $x'y'z'$ system, and ϕ and θ are the azimuthal and polar angles in the $x'y'z'$ system, respectively. The z axis coincides with the propagation axis of the beam. (For more details, see Fig. 1 of Ref. 10.)

The components of the total optical force $\mathbf{F}$ acting on a transparent dielectric sphere can be determined by means of Eq. (1) for a given beam profile and distribution of the incident vectors $\hat{\mathbf{u}}_i(\mathbf{r})$.

The specific expressions used in this work to calculate the different contributions to the total optical force in the case of a Bessel light beam are the following. For $\mathbf{F}^{(\varphi)}$, which is the force contribution due to the incident light rays in the azimuthal direction, we set $\hat{\mathbf{u}}_i = \hat{\boldsymbol{\varphi}}$, and the corresponding components along the x' and y' axes are[10,23]

$$F_{x'}^{(\varphi)} = \frac{R_0^2 n_m}{c}\int_{\pi/2}^{\pi}\int_{\pi}^{2\pi}\frac{I_l(\mathbf{r})\rho_0\sin\phi\sin^2\theta}{\rho}f_\varphi(\mathbf{r}) \times\left[\sin\theta\left(T\frac{R_0}{\rho}\sin\phi - 2R\,\frac{\rho_0\sin\phi\sin\theta\cos\phi}{\rho}\right) + T^2\sum_{k=1}^{N}R^{k-1}(\hat{\mathbf{u}}_{tk})_{x'}^{(\varphi)}\right]\mathrm{d}\phi\mathrm{d}\theta, \tag{7}$$

$$F_{y'}^{(\varphi)} = -\frac{R_0^2 n_m}{c}\int_{\pi/2}^{\pi}\int_{\pi}^{2\pi}\frac{I_l(\mathbf{r})\rho_0\sin\phi\sin^2\theta}{\rho}f_\varphi(\mathbf{r}) \times\left[T\left(\frac{\rho_0 + R_0\sin\theta\cos\phi}{\rho}\right) + 2R\,\frac{\rho_0\sin^2\theta\sin^2\phi}{\rho} - T^2\sum_{k=1}^{N}R^{k-1}(\hat{\mathbf{u}}_{tk})_{y'}^{(\varphi)}\right]\mathrm{d}\phi\mathrm{d}\theta, \tag{8}$$

while the respective z' component is found to be negligible. $I_l(\mathbf{r})$ represents the intensity distribution of the Bessel beam given by Eq. (2).

To calculate $\mathbf{F}^{(z)}$, which is the contribution to the net force due to the incident light rays in the axial direction, we set $\hat{\mathbf{u}}_i = \hat{\mathbf{z}}$, and the incidence angle reduces to $\pi - \theta$. The region of the particle that is illuminated by the axial rays is the lower hemisphere, i.e., $\pi/2 \leqslant \theta \leqslant \pi$ and $0 \leqslant \phi \leqslant 2\pi$. For the x' component of the force, we have now[10,23]

$$F_{x'}^{(z)} = \frac{R_0^2 n_m}{2c}\int_{\pi/2}^{\pi}\int_{0}^{2\pi}I_l(\mathbf{r})f_z(\mathbf{r})\left[-2R\cos\theta\cos\phi + T^2\sum_{k=1}^{N}R^{k-1}(\hat{\mathbf{u}}_{tk})_{x'}^{(z)}\right]\sin 2\theta\mathrm{d}\phi\mathrm{d}\theta. \tag{9}$$

$\mathbf{F}^{(z)}$ has no net component along the y' direction because of the symmetry in the hemispheres defined by $0 < \phi \leqslant \pi$ and $\pi < \phi \leqslant 2\pi$. Finally, the z' component of the force exerted by the axial incident rays is

$$F_{z'}^{(z)} = \frac{R_0^2 n_m}{2c}\int_{\pi/2}^{\pi}\int_{0}^{2\pi}I_l(\mathbf{r})f_z(\mathbf{r})\left[-T + 2R\cos^2\theta + T^2\sum_{k=1}^{N}R^{k-1}(\hat{\mathbf{u}}_{tk})_{z'}^{(z)}\right]\sin 2\theta\mathrm{d}\phi\mathrm{d}\theta. \tag{10}$$

Notice that the Fresnel coefficients R and T, as well as the vectors $\hat{\mathbf{u}}_{tk}$, are not the same in Eqs. (9) and (10) as in Eqs. (7) and (8). A general expression of the vector $\hat{\mathbf{u}}_{tk}$ associated with an arbitrary incident vector can be found in Refs. 10 and 23. To evaluate the Fresnel coefficients R and T, it can be considered that the incident field is composed in equal proportion of rays in the two transverse directions of polarization relative to the plane of incidence for each illuminated element of the sphere, so we take the averages of R and T over the two polarizations.[14,17,19]

For the case of highly reflective metallic particles, the corresponding expressions for the different contributions of the optical force are obtained by substituting $R = 1$ and $T = 0$ in Eqs. (7) and (9).

On the other hand, the only optical torque along the beam axis is generated by the azimuthal component of the force, $\boldsymbol{\tau}_b = [\rho_0 F_\varphi(\rho_0)]\hat{\mathbf{z}}$. But the sphere suffers also a drag torque given by the Stokes equations as $\tau_d = -6\pi\eta\rho_0^2 R_0\omega_p$, where ω_p is the angular velocity of the particle, and η is the viscosity of the surrounding medium. Hence the rotation rate of the particle, $v_p = \omega_p/2\pi$, when both torques are balanced is

$$v_p = \frac{F_\varphi(\rho_0)}{12\pi^2\eta\rho_0 R_0}. \tag{11}$$

The values of ρ_0 correspond to the radial equilibrium positions where the sphere orbits around the center of the beam, and they are numerically determined from the points where the radial force is zero, i.e., $F_\rho(\rho_0) = 0$. It is worth mentioning that, when the particle is centered with respect to the beam axis, Eq. (11) is no longer valid, since the expression for the drag torque is different in that situation, and there is no OAM transfer by scattering to a spherical particle in that case.

ACKNOWLEDGMENTS

We thank Consejo Nacional de Ciencia y Tecnologiá, Mexico, and the Leverhulme Trust, the UK Engineering and Physical Sciences Research Council, for their support of our work. K. Volke-Sepúlveda acknowledges INAOE for support during the development of this paper.

Karen Volke-Sepúlveda may be reached by e-mail at karen@fisica.unam.mx.

REFERENCES

1. L. Allen, M. W. Beijersbergen, R. J. C. Spreeuw, and J. P. Woerdman, “Orbital angular momentum of light and the transformation of Laguerre–Gaussian laser modes,” Phys. Rev. A **45**, 8185–8189 (1992).
2. R. Horak, Z. Bouchal, and J. Bajer, “Non-diffracting stationary electromagnetic field,” Opt. Commun. **133**, 315–327 (1997).
3. K. P. Volke-Sepúlveda, V. Garcés-Chávez, S. Chávez-Cerda, J. Arlt, and K. Dholakia, “Orbital angular momentum of a high-order Bessel light beam,” J. Opt. B: Quantum Semiclass. Opt. **4**, S82–S89 (2002).
4. J. Durnin, J. J. Miceli, and J. H. Eberly, “Diffraction-free beams,” Phys. Rev. Lett. **58**, 1499–1501 (1987).
5. S. Chávez-Cerda, “A new approach to Bessel beams,” J. Mod. Opt. **46**, 923–930 (1999).
6. A. Ashkin, J. M. Dziedzic, J. Bjorkholm, and S. Chu, “Observation of a single-beam gradient force optical trap for dielectric particles,” Opt. Lett. **11**, 288–290 (1986).
7. H. He, M. E. J. Friese, N. R. Heckenberg, and H. Rubinsztein-Dunlop, “Direct observation of transfer of angular momentum to absorptive particles from a laser beam with a phase singularity,” Phys. Rev. Lett. **75**, 826–829 (1995).
8. M. E. J. Friese, J. Enger, H. Rubinsztein-Dunlop, and N. R. Heckenberg, “Optical angular-momentum transfer to trapped absorbing particles,” Phys. Rev. A **54**, 1593–1596 (1996).
9. N. B. Simpson, K. Dholakia, L. Allen, and M. J. Padgett, “Mechanical equivalence of spin and orbital angular momentum of light: an optical spanner,” Opt. Lett. **22**, 52–54 (1997).
10. V. Garcés-Chávez, K. Volke-Sepúlveda, S. Chávez-Cerda, W. Sibbett, and K. Dholakia, “Orbital angular momentum transfer to an optically trapped low-index particle,” Phys. Rev. A **66**, 063402 (2002).
11. M. V. Berry, “Much ado about nothing: optical distortion lines (phase singularities, zeros, and vortices),” in *International Conference on Singular Optics*, M. S. Soskin, ed., Proc. SPIE **3487**, 6 (1998).
12. A. T. O’Neil, I. MacVicar, L. Allen, and M. J. Padgett, “Intrinsic and extrinsic nature of the orbital angular momentum of a light beam,” Phys. Rev. Lett. **88**, 053601 (2002).
13. V. Garcés-Chávez, D. McGloin, M. J. Padgett, W. Dultz, H. Schmitzer, and K. Dholakia, “Observation of the transfer of the local angular momentum density of a multi-ringed light beam to an optically trapped particle,” Phys. Rev. Lett. **91**, 093602 (2003).
14. G. Roosen and C. Imbert, “Optical levitation by means of two horizontal laser beams: a theoretical and experimental study,” Phys. Lett. A **59**, 6–8 (1976).
15. J. S. Kim and S. S. Lee, “Scattering of laser beams and the optical potential well for a homogeneous sphere,” J. Opt. Soc. Am. **73**, 303–312 (1983).
16. A. Ashkin, “Forces of a single-beam gradient trap on a dielectric sphere in the ray optics regime,” Biophys. J. **61**, 569–582 (1992).
17. R. Gussgard, T. Lindmo, and I. Brevik, “Calculation of the trapping force in a strongly focused laser beam,” J. Opt. Soc. Am. B **9**, 1922–1930 (1992).
18. R. C. Gauthier and S. Wallace, “Optical levitation of spheres: analytical development and numerical computations of the force equations,” J. Opt. Soc. Am. B **12**, 1680–1686 (1995).
19. S. Nemoto and H. Togo, “Axial force acting on a dielectric sphere in a focused laser beam,” Appl. Opt. **37**, 6386–6394 (1998).
20. M. Mansuripur, “Geometric-optical rays, Poynting’s vector and field momenta,” Opt. Photonics News **10**(3), 53–56 (1999).
21. J. Courtial and M. J. Padgett, “Limit to the orbital angular momentum per unit energy in a light beam that can be focused onto a small particle,” Opt. Commun. **173**, 269–274 (2000).
22. J. C. Gutierrez-Vega, M. D. Iturbe-Castillo, and S. Chavez-Cerda, “Alternative formulation for invariant optical fields: Mathieu beams,” Opt. Lett. **25**, 1493–1495 (2000).
23. Karen Volke-Sepulveda, “Light beams with angular momentum and applications in optical tweezers,” Ph.D. thesis (Instituto Nacional de Astrofísica, Optica y Electroníca, Puebla, Mexico, 2003).
24. J. Arlt, K. Dholakia, J. Soneson, and E. M. Wright, “Optical dipole traps and atomic waveguides based on Bessel light beams,” Phys. Rev. A **63**, 063602 (2001).
25. J. Arlt, V. Garcés-Chávez, W. Sibbett, and K. Dholakia, “Optical micromanipulation using a Bessel light beam,” Opt. Commun. **197**, 239–245 (2001).
26. A. Ashkin and J. M. Dziedzic, “Stability of optical levitation by radiation pressure,” Appl. Phys. Lett. **24**(12), 586–588 (1974).
27. M. P. MacDonald, G. C. Spalding, and K. Dholakia, “Microfluidic sorting in an optical lattice,” Nature (London) **426**, 421–424 (2003).
28. K. Ladavac, K. Kasza, and D. G. Grier, “Sorting by periodic potential energy landscapes: optical fractionation,” Phys. Rev. E (to be published).